

A multiwavelength study of young massive star forming regions: II. The dust environment

Guido Garay

Departamento de Astronomía, Universidad de Chile, Casilla 36-D, Santiago, Chile

Diego Mardones

Departamento de Astronomía, Universidad de Chile, Casilla 36-D, Santiago, Chile

Kate J. Brooks

Australia Telescope National Facility, P.O. Box 76, Epping NSW 1710, Australia

Liza Videla

Departamento de Astronomía, Universidad de Chile, Casilla 36-D, Santiago, Chile

and

Yanett Contreras

Departamento de Astronomía, Universidad de Chile, Casilla 36-D, Santiago, Chile

ABSTRACT

We present observations of 1.2-mm dust continuum emission, made with the Swedish ESO Submillimeter Telescope, towards eighteen luminous IRAS point sources, all with colors typical of compact H II regions and associated with CS(2→1) emission, thought to be representative of young massive star forming regions. Emission was detected toward all the IRAS objects. We find that the 1.2-mm sources associated with them have distinct physical parameters, namely sizes of ~ 0.4 pc, dust temperatures of ~ 30 K, masses of $\sim 2 \times 10^3 M_{\odot}$, column densities of $\sim 3 \times 10^{23} \text{ cm}^{-2}$, and densities of $\sim 4 \times 10^5 \text{ cm}^{-3}$. We refer to these dust structures as massive and dense cores. Most of the 1.2-mm sources show single-peaked structures, several of which exhibit a bright compact peak surrounded by a weaker extended envelope. The observed radial intensity profiles of sources with this type of morphology are well fitted with power-law intensity

profiles with power-law indices in the range 1.0 – 1.7. This result indicates that massive and dense cores are centrally condensed, having radial density profiles with power-law indices in the range 1.5 – 2.2. We also find that the UC HII regions detected with ATCA towards the IRAS sources investigated here (Paper I) are usually projected at the peak position of the 1.2-mm dust continuum emission, suggesting that massive stars are formed at the center of the centrally condensed massive and dense cores.

Subject headings: ISM: clouds — ISM: dust — stars: formation — stars: massive

1. Introduction

The birth process and early evolution of massive stars is currently one of the most debated subjects in astrophysics. To achieve a better understanding of the formation processes of high-mass stars it is essential to know the physical conditions of the parental cloud which are thought to play a critical role in determining the formation mechanism. Accordingly, during the last decade intense observational efforts have been carried out to determine the characteristics of the molecular gas (e.g., Plume et al. 1992, 1997; Juvela 1996; Shirley et al. 2003) and dust (e.g., Beuther et al. 2002; Mueller et al. 2002; Faúndez et al. 2004; Williams et al. 2004) associated with massive star forming regions.

In this regard we are carrying out a multi-wavelength study of a sample of 18 luminous IRAS sources in the southern hemisphere thought to be representative of young massive star forming regions. The goal is to understand the physical and chemical differences between different stages of early evolution. The objects were taken from the Galaxy-wide survey of CS(2→1) emission towards IRAS sources with IR colors typical of compact H II regions (Bronfman, Nyman, & May 1996). We selected sources based primarily on the observed CS(2→1) line profiles; looking for self-absorbed lines consistent with inward or outward motions (e.g., Mardones 1998), and/or with extended line wings, possibly indicating the presence of bipolar outflows. In addition, the sources were required to have IRAS 100 μ m fluxes greater than 10^3 Jy and to be in the southern hemisphere ($\delta < -20^\circ$). The luminosity of the IRAS sources, computed using the IRAS energy distribution and distances derived by Bronfman (2006, private communication) are in the range $1 \times 10^4 - 4 \times 10^5 L_\odot$, implying that they contain at least an embedded massive star.

Here we report the results of 1.2-mm continuum observations, made with the Swedish ESO Submillimeter Telescope with angular resolution of $24''$, toward all objects in our sample. The 1.2-mm emission was mapped within regions of $\sim 15' \times 10'$ centered on the IRAS

sources. The primary goal of these observations was to determine the characteristics and physical conditions of the dust and gas clouds harboring recently formed massive stars. The characteristics of the ionized gas associated with the IRAS sources in our sample is reported in the first paper of the series (Garay et al. 2006; Paper I).

2. Observations

The observations were made using the 15 m Swedish–ESO Submillimetre Telescope (SEST) located on La Silla, Chile. The 1.2-mm continuum observations were made using the 37-channel SEST Imaging Bolometer Array (SIMBA) during October, 2001 and July 2002. The passband of the bolometers has an equivalent width of 90 GHz and is centered at 250 GHz. The HPBW of a single element is $24''$ and the separation between elements on the sky is $44''$. We observed in the fast mapping mode, using a scan speed of $80'' \text{ s}^{-1}$. Each observing block consisted of 50 scan lines in azimuth of length $800''$ and separated in elevation by $8''$, giving a map size of $400''$ in elevation. This block required ~ 15 minutes of observing time. We observed 2–4 blocks per source, achieving rms noise levels of typically 50 mJy beam^{-1} . The data were reduced according to a standard procedure using the software package MOPSI, which included baseline subtraction and rejection of correlated sky-noise. Flux calibration was performed using a sky-opacity correction and a counts-to-flux conversion factor derived from maps of Uranus. Uncertainties in the absolute calibration and pointing accuracy are estimated at 20% and $3''$, respectively. The observed sources are listed in Table 1. The noise level achieved in the images is given in column 4.

3. Results

Figures 1-3 present maps of the 1.2-mm emission, towards all the observed targets, within regions of typically $5' - 7'$ in size. The filled stars and open triangles indicate, respectively, the peak position of the compact and more diffuse regions of ionized gas detected with ATCA within the mapped regions (Paper I). In a few panels we have also indicated, with open asterisks, the peak position of the sources detected in the *Midcourse Space Experiment* (MSX; Price 1995) survey of the Galactic plane (Egan et al. 1998) at $21.3 \mu\text{m}$. We will refer to these as MSX-E band sources, most of which are likely to signpost the presence of embedded energy sources.

Continuum 1.2-mm emission was detected toward the eighteen IRAS sources. The observed parameters of the 1.2-mm sources as a whole are given in Table 2. Cols.(2) and

(3) give their peak position. Cols.(4) and (5) give, respectively, the peak flux density and the total flux density, the later measured directly from the maps using the AIPS tasks IMEAN. Col.(6) gives the deconvolved major and minor FWHM angular sizes determined by fitting a single Gaussian profile to the entire source. Col.(7) gives a description of the source morphology. The *c+e* morphology is used to describe a source with a brightness distribution showing a bright compact peak surrounded by a weaker extended envelope. The criteria for classifying a source in this category is as follows. A single Gaussian fit has to produce distinctive residuals, consisting of a central positive peak surrounded by a ring of negative values and further out a ring of positive values. This is what is expected when a power law profile is fitted with a single Gaussian profile. On the other hand, two Gaussian fits – a compact bright component plus an extended weaker component surrounding the former – has to produce reasonable fits with the central position of both components being coincident within the observational errors. Thus the *c+e* sources should also be understood as sources in which the brightness distribution follows a power-law dependence with radius. For sources with multiple or complex morphology we fitted the brightness distribution using the minimum number of Gaussian components that produce residuals that are consistent with the noise level in the maps. The observed parameters of the fitted components are given in Table 3. Here flux densities and angular sizes corresponds to the values obtained by the fitting process using the AIPS task JMFIT. In what follows we discuss the characteristics of the 1.2-mm emission toward each of the IRAS sources, individually.

3.1. Individual sources

IRAS 12383-6128 (G301.731+1.104).—The 1.2-mm emission towards IRAS 12383-6128 (see Fig. 1a) arises from an extended region with an irregular morphology, showing at least four peaks. The whole region has deconvolved major and minor axis of, respectively, $116''$ and $72''$, and a total flux density of 13.4 Jy. The morphology of the region was best fit as being produced by four compact components (labeled A, B, C and D) and an extended halo. The sizes and radius of the individual components are given in Table 3. The compact cometary-like HII region detected with ATCA lies at the center of the dust core and is associated with the brighter 1.2-mm component (C).

IRAS 13291-6249 (G307.560-0.586).—The 1.2-mm emission towards IRAS 13291-6249 (see Fig. 1b) arises from a bright compact component and a weak, extended, irregular component. The total flux density of the region is 8.5 Jy. The compact cometary-like HII region detected with ATCA lies at the peak position of the dust core.

IRAS 14095-6102 (G312.596+0.048).—The 1.2-mm emission towards IRAS 14095-6102

(see Fig. 1c) arises from a single structure, with a $c+e$ morphology. The total flux density of the region is 6.7 Jy. The compact HII region detected with ATCA lies near the peak position of the dust core.

IRAS 14593-5852 (G319.163-0.419).—The 1.2-mm emission towards IRAS 14593-5852 (see Fig. 1d) arises from an unresolved bright compact component (labeled B), with a flux density of 0.88 Jy, and a weaker extended component (labeled A) with deconvolved major and minor axis of $90''$ and $54''$, respectively. The total flux density of the region is 11.3 Jy. The compact HII region detected with ATCA lies at the peak position of the dust core.

IRAS 15394-5358 (G326.474+0.697).—The 1.2-mm emission towards IRAS 15394-5358 (see Fig. 1e) arises from a single structure, with a $c+e$ morphology. The total flux density of the region is 15.9 Jy. No radio continuum emission was detected with ATCA towards this dust core up to a 3σ level of 0.5 mJy at 8.6 GHz.

IRAS 15502-5302 (G328.307+0.432).—The 1.2-mm emission towards IRAS 15502-5302 (see Fig. 1f) arises from a bright compact component and a weaker extended component. The later has deconvolved major and minor axis of, respectively, $131''$ and $73''$. The total flux density of the region is 27.3 Jy. The two compact HII regions detected with ATCA (radio components A and B; peak indicated by filled stars) lie near the peak position of the compact component, which is also associated with the brighter of the two MSX-E sources detected towards the region. The four more diffuse HII regions (radio components C, D, E, and F; peak positions indicated by open triangles) are located within the extended component. The weak protuberance of 1.2-mm emission seen to the west is associated with the second MSX-E source.

IRAS 15520-5234 (G328.808+0.632).—The 1.2-mm emission towards IRAS 15520-5234 (see Fig. 2a) arises from a single structure exhibiting a $c+e$ morphology. The extended emission has deconvolved major and minor axis of $100''$ and $77''$, respectively. The total flux density of the region is 27.0 Jy. The two compact HII regions detected with ATCA lie at the peak position of the dust core.

IRAS 15596-5301 (G329.404-0.457).—The 1.2-mm emission towards IRAS 15596-530 (see Fig. 2b) arises from a single structure, with roughly a $c+e$ morphology. The total flux density of the region is 8.3 Jy. The three compact HII regions detected with ATCA (Garay et al. 2002) lie near the peak position of the dust core.

IRAS 16128-5109 (G332.153-0.445).—The 1.2-mm emission within the region shown in panel (c) of Fig. 2 arises from two distinct sources. The eastern source, associated with IRAS 16128-5109, exhibits a $c+e$ morphology. The extended emission has deconvolved major and minor axis of $106''$ and $77''$, respectively. The entire eastern source has a total flux density of

19.9 Jy. The brighter component of the complex region of ionized gas detected with ATCA (peak indicated by a filled star) lies at the peak of the core, which is also associated with the brighter of the two MSX-E sources detected towards the region (indicated by asterisks). The three more diffuse HII regions (radio components a, b, and d; peak positions indicated by open triangles) are located within the halo. The western 1.2-mm source, referred as 16128-West in Table 2, exhibits a Gaussian morphology, with deconvolved major and minor axis of 48'' and 41'', respectively, has a flux density of 6.8 Jy, and it is associated with the second MSX-E source detected in the field.

IRAS 16272-4837 (G335.582-0.284).—The 1.2-mm emission towards IRAS 16272-4837 (see Fig. 2d) arises from a single structure consisting of a bright central component and a weak, extended irregular component showing elongations to the west and north-west. The total flux density of the region is 13.9 Jy. No radio continuum emission was detected towards this core up to a level of 0.2 mJy at 4.8 GHz (Garay et al. 2002).

IRAS 16458-4512 (G340.248-0.373).—The 1.2-mm emission within the region shown in panel (e) of Fig. 2 arises from two distinct extended regions. The region to the southwest, associated with IRAS 16458-4512, exhibits an irregular morphology, with at least two components (labeled A and B). The fitted parameters of the individual components are given in Table 3. Both components are associated with energy sources detected by MSX in the E band. The compact HII region detected with ATCA lies at the peak position of the brighter 1.2-mm component (component B), indicating it harbors a more luminous object than component A.

The northeast region, which exhibits a C-shape like morphology, is not associated with MSX sources and appears in silhouette against the background emission in the MSX-A band, suggesting it corresponds to a cold filamentary structure with large column densities.

IRAS 16524-4300 (G342.704+0.130).—The 1.2-mm emission towards IRAS 16524-4300 (see Fig. 2f) arises from a single structure with a *c+e* morphology. The extended emission has deconvolved major and minor axis of, respectively, 122'' and 80''. The total flux density of the region is 11.1 Jy. The two compact HII regions detected with ATCA lie near the peak position of the bright compact component.

IRAS 16547-4247 (G343.126-0.062).—The 1.2-mm emission towards IRAS 16547-4247 (see Fig. 3a) arises from a single structure which exhibits a *c+e* morphology. The total flux density of the region is 20.8 Jy. Radio continuum observations towards this core show the presence of a triple radio source. The central radio component (shown as a triangle) correspond to a thermal jet and is located at the peak position of the dust core.

IRAS 17008-4040 and 17009-4042 (G345.499+0.354 and G345.490+0.311).—The 1.2-mm

emission within the region shown in panel (b) of Fig. 3 arises from an extended elongated structure exhibiting two components. The northern component, associated with IRAS 17008-4040, shows a $c+e$ morphology. It has deconvolved major and minor axis of, respectively, $102''$ and $57''$, and a flux density of 34.1 Jy. The brighter of the two MSX-E sources detected near the northern component lies at the peak position of the 1.2-mm emission. No radio emission was detected towards this peak position up to a 3σ level of 1.5 mJy at 4.8 GHz. The extended HII region detected with ATCA towards IRAS 17008-4040 (peak position indicated by an open triangle) is displaced towards the east from the peak position of the 1.2-mm emission, by $\sim 30''$, and is coincident with the second MSX-E source.

The southern 1.2-mm component, associated with IRAS 17009-4042, exhibits a Gaussian brightness distribution with deconvolved major and minor axis of $49''$ and $34''$, respectively, and a flux density of 44.8 Jy. The compact HII region detected with ATCA lies at the peak position of the 1.2-mm emission, which is also associated with the brighter of the two MSX-E sources detected near this component.

IRAS 17016-4124 (G345.001-0.220).—The 1.2-mm emission within the region shown in panel (c) of Fig. 3 arises from two distinct sources. The northern object, with a total flux density of 45.0 Jy, consists of an extended filamentary structure with a bright compact component at its southern end. The filament has deconvolved major and minor axis of $308''$ and $95''$, respectively, and a flux density of 33.9 Jy. The compact core, associated with IRAS 17016-4124, has deconvolved major and minor axis of $24''$ and $21''$, respectively, and a flux density of 13.7 Jy. The compact HII region detected with ATCA lies at the peak position of the compact core, which is also associated with the brighter of the three MSX-E sources detected within the region.

The southern 1.2-mm object, referred as 17016-South in Table 2, exhibits an irregular morphology, with deconvolved major and minor axis of $89''$ and $85''$, respectively, and a flux density of 6.5 Jy. It is associated with the other two MSX-E objects detected within the region.

IRAS 17158-3901 (G348.534-0.973).—The 1.2-mm emission towards IRAS 17158-3901 (see Fig. 3d) show complex morphology, which can be decomposed as arising from at least three components. The total flux density of the entire source is 26.7 Jy. The western component (labeled A) has deconvolved major and minor axis of $179''$ and $35''$, respectively, and a flux density of 11.2 Jy. Component A is associated with the HII region detected with ATCA and with the brighter of the two MSX-E band sources in the field. The southern component (labeled B) has deconvolved major and minor axis of $76''$ and $49''$, respectively, and a total flux density of 11.5 Jy. The eastern component (labeled C), the brighter of the 1.2-mm components (peak flux of 3.0 Jy/beam), has deconvolved major and minor axis of

30" and 24", respectively, and a total flux density of 6.3 Jy. It is associated, although not coincident, with the second MSX-E source detected in the field.

IRAS 17271-3439 (G353.410-0.367).—The 1.2-mm emission toward IRAS 17271–3439 (see Fig. 3e) arises from a bright compact central component and an elongated weak extended component. The total flux density measured within the whole region is 89 Jy. The compact component has deconvolved major and minor angular diameters of 37" and 21", respectively, and a flux density of 18 Jy. The extended component has deconvolved major and minor angular diameters of 169" and 84", and a flux density of 65 Jy. The ultra compact HII region detected with ATCA is coincident, within the errors, with the 1.2-mm peak position.

Projected toward the dust cloud lie the two 1.4 GHz radio sources (peak positions marked by the crosses) detected by the NRAO VLA Sky Survey (NVSS; Condon et al. 1998) within the $7 \times 7'$ region of the sky shown in Fig. 3e. The northern NVSS source corresponds to the shell-like HII region detected with ATCA at 1.4 GHz, and is associated with the IRAS source (peak position marked by the triangle). The southern NVSS source is an extended HII region, with angular diameters of $88.7'' \times 74.0''$ and is resolved out in our ATCA radio observations (paper I).

4. Discussion

4.1. Structure of the dust cores

Most of the 1.2-mm sources associated with the IRAS objects exhibit single-peaked structures. In only four cases (IRAS 12383-6128, 14593-5852, 16458-4512, and 17158-3901) we see evidence for the presence of multiple components. To discern whether the lack of clustering is due to intrinsic reasons, such as the absence of fragmentation, or due to the coarse angular resolution of the present observations requires observations with high angular resolution.

An important observational evidence that bears on the physical structure of the cores, is the fact that most of the single-peaked objects show *c+e* morphologies, with clear centrally condensed peaks. This is illustrated in Figure 4 which shows slices of the observed 1.2-mm intensity across the ten sources with *c+e* morphologies. We find that the observed radial intensity profiles can be well fitted (see dotted lines) with single power-law intensity profiles of the form $I \propto r^{-\alpha}$, where r is the distance from the center, properly convolved with the beam of 24". The fitted power-law indices are in the range from 1.0 to 1.7.

Assuming that cores have density and temperature radial distributions following power

laws, then for optically thin dust emission the intensity index α is related to the density index p ($n \propto r^{-p}$) and the temperature index q ($T \propto r^{-q}$), by the expression $\alpha = p + Qq - 1$ (Adams 1991; Motte & André 2001), where Q is a temperature and frequency correction factor with a value of ~ 1.2 at 1.2-mm and 30 K (Beuther et al. 2002). Most of the massive and dense cores investigated here are heated by a luminous energy source embedded at their central position, as signposted by the presence of either a compact H II region or an MSX-E source. van der Tak et al. (2000) have found that for sources with similar characteristics the temperature decreases with distance following a power-law with an index of 0.4. Adopting this value for q , we then infer, using the above expression, that massive and dense cores have density distributions with power-law indices in the range 1.5 – 2.2, with an average value of 1.8.

Several dust continuum studies have already shown the presence of steep density gradients within massive and dense cores (e.g., van der Tak et al. 2000, Mueller et al. 2002, Beuther et al. 2002, Williams et al. 2005). The density dependence with radius can be approximated by power-law distributions with average values of p in the range between 1.3 and 1.8, similar to the values derived in this work. The individual values of p exhibit, however, a large spread, which is likely to reflect the presence of clumpiness and fragmentation within massive and dense cores (e.g., Molinari et al. 2002; Beuther & Schilke 2004). Differences in the fragmentation process of varying cores has been already pointed out by Beuther et al. (2005).

4.2. Overall parameters of the dust cores

The parameters derived from the 1.2-mm observations are summarized in Table 4. As distances [col. (2)] we adopted the kinematic distances provided by Bronfman (2006, private communication) determined using a rotation curve with an orbital velocity of 220 km s⁻¹ at 8.5 kpc from the Galactic center (Brand 1986). The dust temperatures given in col. (3) correspond to the colder temperature determined from fits to the spectral energy distribution (SED) which included flux densities at wavelengths of 12, 25, 60 and 100 μm (IRAS data), 8.3, 12.1, 14.7, and 21.3 μm (MSX data), 3.6, 4.5, 5.8 and 8.0 μm (Spitzer data), and 1.2-mm (SIMBA data). We find that to achieve a good fit of the SED in this wide wavelength range (4 to 1200 μm) at least three temperature components are needed (Morales et al. 2007; paper III). For the single peaked cores, the radius given in col. (4) were computed from the geometric mean of the deconvolved major and minor angular sizes obtained from single Gaussian fits to the observed spatial structure. The masses [col. (5)] were computed following Chini, Krügel, & Wargau (1987), adopting a dust opacity at 1.2-mm of 1 cm² g⁻¹ (Ossenkopf

& Henning 1994), a dust-to-gas mass ratio of 0.01, and using the dust temperatures derived from the fit of the SED. Cols. (6) and (7) give, respectively, the average column densities and average molecular densities derived from the masses and radius assuming that the cores have uniform densities. Clearly, this is a rough simplification, since as discussed in section 4.1 massive and dense cores are likely to have steep density gradients. Finally, the continuum optical depth at 1.2-mm is given in col. (8).

Figure 5 shows a histogram with the distribution of the radius, masses, and densities of the cores in our sample. We find that the dust cores harboring recently formed massive stars have typically sizes of ~ 0.4 pc, masses of $\sim 2 \times 10^3 M_{\odot}$, column densities of $\sim 3 \times 10^{23} \text{ cm}^{-2}$, densities of $\sim 4 \times 10^5 \text{ cm}^{-3}$, and dust temperatures of 30 K. A comparison with values of other cores containing young massive stars derived from molecular line observations (e.g., Cesaroni et al. 1991, Juvela 1996, Plume et al. 1997) shows good agreement. For instance, from a survey of molecular emission, in several transitions of CS, toward massive star forming regions associated with water masers, Plume et al. (1997) found that high-mass stars are formed in molecular cores with typical radii of 0.5 pc, densities of $8 \times 10^5 \text{ cm}^{-3}$, and virial masses of $4 \times 10^3 M_{\odot}$. Clearly the 1.2-mm dust continuum and high density molecular line emissions are tracing the same structures. We conclude that massive stars are formed in regions of molecular gas and dust with distinctive physical characteristics, which we have referred to as the maternities of massive stars (Garay 2005).

4.3. High-mass star formation within the massive and dense cores

Given their large masses, of typically $2 \times 10^3 M_{\odot}$, the overall collapse process of massive and dense cores is likely to produce a protostar cluster. The questions of how an individual massive star forms and how the cluster forms are therefore closely related. The derived properties of massive and dense cores are then important boundary conditions to be taken into account for models and simulations. The physical conditions of the massive and dense cores with embedded high-mass stars, as the ones investigated here, do in fact correspond to the initial conditions for star cluster formation (Garay et al. 2004), except for the temperatures. In massive and dense cores without embedded high-mass stars the temperatures are typically 15 K (Menten, Pillai, & Wyrowski 2005; Shridharan et al. 2005), whereas in massive and dense cores with internal energy sources the temperatures are typically 32 K (Faúndez et al. 2004).

Using the results of the 1.2-mm dust continuum observations reported here and the radio continuum observations reported in Paper I, we can address the basic question of Where are massive stars formed within protocluster cores? This is a relevant question because the

location of high-mass stars within massive and dense cores may shed some light on their formation mechanism. Figures 1-3 strikingly show that in massive and dense cores associated with regions of ionized gas, implying that they have ongoing massive star formation, the compact H II regions are usually found projected at the peak of the dust continuum emission. This is illustrated in Figure 6 which shows a histogram of the distribution of the linear offsets of the compact H II region from the peak position of the associated 1.2-mm core. We find that of the eighteen compact H II regions plotted in Figs 1-3, twelve are coincident, within the errors, with the peak of the 1.2-mm emission and that all them are located within 0.4 pc, which is the average radius of the dust cores. In addition, the thermal jet associated with IRAS16547-4247 is also located at the peak of the 1.2-mm emission. The dotted line in Fig. 6 indicates the expected distribution if the compact H II regions were uniformly distributed across the dust core. The observed distribution clearly shows that massive stars are preferentially born at the center of massive and dense cores.

Two different mechanisms have been proposed to explain the formation of massive stars: accretion (Osorio, Lizano, & D’Alessio 1999; Yorke & Sonnhalter 2002; McKee & Tan 2003) and mergers (Bonnell, Bate, & Zinnecker 1998; Bonnell 2002; Zinnecker & Bate 2002). In these two main theoretical ideas, the birth of massive stars is envisioned as an event associated with a very dense environment. In the merger model the determining parameter is the stellar density whereas in the accretion model it is the gas density. In the merger scenario (see review by Stahler, Palla, & Ho 2000) it is proposed that high-mass stars form by the merging of low and intermediate mass protostars in a dense cluster environment. Observable consequences of both scenarios for massive star formation have been thoroughly discussed by Bally & Zinnecker (2005).

Are the observational data presented in this paper able to discriminate between the two competing scenarios of high-mass star formation? In recollection, our observations show that high-mass stars tend to form at the center of massive ($\sim 2 \times 10^3 M_{\odot}$), dense ($\sim 4 \times 10^5 \text{ cm}^{-3}$) and turbulent ($\Delta v \sim 4 \text{ km s}^{-1}$) molecular cores which exhibit steep density profiles (typically $n \propto r^{-1.8}$). In addition, we find that the virial mass of the cores, determined from molecular line observations, and the mass determined from dust continuum observations are in very good agreement. This indicates that most of the core mass appear to be in the form of molecular gas.

Lets first consider the merger hypothesis. The process of building up massive stars by collisions with lower mass objects is more efficient at the center of the cluster, where considerable more dynamical interactions take place. The merger hypothesis then predicts that high-mass stars should be found at the center of the cluster, in accord with the finding that UC H II regions are usually located at the center of the cores. However, for stellar

mergers to be responsible for the formation of massive stars stellar densities of $\geq 10^8$ stars pc^{-3} are required (Bonnell 2002). These are more than four orders of magnitude larger than the stellar volume densities derived in young embedded dense clusters of $\leq 10^4$ stars/ pc^3 (Megeath et al. 1996; Carpenter et al. 1997). From numerical simulations of the collapse of a $10^3 M_\odot$ fragmenting turbulent molecular core, Bonnell et al. (2003) argued that stellar densities of $10^6 - 10^8$ stars pc^{-3} are achieved during a brief period of time and suggested that it is during this transient ultradense and highly embedded phase that mergers take place. The final state of their simulation (after 2.4 initial free-fall times) shows a centrally condensed cluster, with the fraction of mass in stars being 84%. This prediction is at variance with our observations which shows that even though high-mass stars have already been formed at the center of massive cores, most of the total mass is still in the form of molecular gas. It is possible that in cores with steep density profiles, as the ones investigated here, the fragmentation process is not very efficient. In addition mergers are expected to generate luminous infrared flares, poorly collimated impulsive outflows, transient thermal and non-thermal ultracompact radio sources (Bally & Zinnecker 2005), which find little observational support.

The accretion hypothesis requires that the parental cores be dense enough such that upon collapse the ram pressure of the associated accretion inflow overcame the radiative forces on dust. McKee & Tan (2002; 2003) have proposed that massive stars are formed in centrally condensed turbulent cores. The high degree of concentration prevent fragmentation and the accretion rate onto a growing protostar at their centers are high enough to overwhelm its radiation pressure producing a massive star. We find that the cores investigated here have very high mean pressures ($P/k \sim 5 \times 10^8 \text{ K cm}^{-3}$), large effective sound speeds ($a_{eff} \sim 1.9 \text{ km s}^{-1}$) and high column densities ($3 \times 10^{23} \text{ cm}^{-2}$), which are the required conditions for high-mass stars to growth by accretion. This observational evidence strongly suggest that the cradles of massive stars are formed by direct accretion at the center of centrally condensed massive and dense cores as hypothesized by McKee & Tan (2003). In their turbulent and pressurized dense core accretion model, the collapse of a massive and dense core is likely to produce the birth of a stellar cluster, with most of the mass going into relatively low-mass stars. The high-mass stars are formed preferentially at the center of the core, where the pressure is the highest, and in short time scales of $\sim 10^5$ yrs (Osorio et al. 1999; McKee & Tan 2002).

With regard to the small observed size of the UC H II regions, Keto (2002) has shown that a newly formed massive star within a dense molecular core may initially produce a confined region of ionized gas. The gravitational attraction of the massive central star can maintain a steep density gradient and accretion flow within the ionized gas and prevents the H II region from expanding hydrodynamically. In paper I we suggested that the main

mechanism of confinement of the UC H II regions in our sample, which are excited by stars with an output of UV photons of typically $\leq 3 \times 10^{48} \text{ s}^{-1}$, is provided by the high density and large turbulent pressure of the surrounding molecular gas. Under these conditions they reach pressure equilibrium in very short times, of $\sim 5 \times 10^3$ yrs, having equilibrium radius of typically ~ 0.03 pc. With the currently available data it is not possible to address the question of whether or not the formation of high-mass and low-mass stars in the massive and dense cores investigated here is coeval. It might be possible that the most massive stars are formed first at their center, either as a single object or in small groups, followed then by low-mass star formation that is triggered by the feedback effects (stellar winds, ionization, compression) of the young high-mass stars at the core center.

5. Summary

We made 1.2-mm continuum observations, using SIMBA at the SEST, towards eighteen luminous IRAS point sources with colors of UC H II regions and CS(2-1) emission. These are thought to be massive star forming regions in early stages of evolution. The objectives were to determine the characteristics and physical properties of the dust clouds in which high-mass stars form. Our main results and conclusions are summarized as follows.

Continuum emission was detected toward all the observed targets. We find that the 1.2-mm sources associated with the luminous IRAS objects, which we refer to as massive and dense cores, have distinct physical parameters, namely linear radius of ~ 0.4 pc, dust temperatures of ~ 30 K, masses of $\sim 2 \times 10^3 M_{\odot}$, column densities of $\sim 3 \times 10^{23} \text{ cm}^{-2}$, and densities of $\sim 4 \times 10^5 \text{ cm}^{-3}$.

Most of the 1.2-mm sources in our sample have single-peaked structures. In addition, several of them exhibit core-halo morphologies, indicating the presence of steep gradients in their densities. The observed radial intensity profiles are well modeled with intensity profiles following power-law dependences with radius with indices in the range 1.0 – 1.7. This in turn implies that massive and dense cores are centrally condensed, with the density decreasing outwards with radius, r , as $n \propto r^{-p}$, with p in the range 1.5 – 2.2.

We find that most of the compact H II regions detected with ATCA towards our sample of IRAS objects are located at the peak position of the massive and dense cores. This is consistent with the hypothesis that the formation of massive stars proceeds via accretion in the central regions of very dense and massive cores. Under these conditions the regions of ionized gas reach pressure equilibrium with their dense and turbulent molecular surroundings in only $\sim 3 \times 10^3$ yrs. The high density and large turbulent pressure of the molecular gas

surrounding UC H II regions is therefore the main mechanism of their confinement.

G.G. and D.M. gratefully acknowledge support from the Chilean *Centro de Astrofísica* FONDAP No. 15010003.

REFERENCES

- Adams, F.C. 1991, *ApJ*, 382, 544
- Bally, J., & Zinnecker, H. 2005, *AJ*, 129, 2281
- Beuther, H., & Schilke, P. 2004, *Science*, 303, 1167
- Beuther, H., Schilke, P., Menten, K. M., Motte, F., Sridharan, T. K., & Wyrowski, F. 2002, *ApJ*, 566, 945
- Beuther, H., Zhang, Q., Sridharan, T. K., & Chen, Y. 2005, *ApJ*, 628, 800
- Bonnell, I.A. 2002, in *ASP Conf. Ser. Vol. 267, The Earliest Stages of Massive Star Birth*, ed. P.A. Crowther (San Francisco: ASP), 193
- Bonnell, I.A., Bate, M.R., & Zinnecker, H. 1998, *MNRAS*, 298, 93
- Brand, J. 1986, Ph.D. thesis, Leiden University
- Bronfman, L., Nyman, L.-Å., & May, J. 1996, *A&AS*, 115, 81
- Carpenter, J.M., Meyer, M.R., Dougados, C., Strom, S.E., & Hillenbrand, L.A. 1997, *AJ*, 114, 198
- Cesaroni, R., Walmsley, C.M., Kömpe, C., & Churchwell, E. 1991, *A&A*, 252, 278
- Chini, R., Krügel, E., & Wargau, W. 1987, *A&A*, 181, 378
- Condon, J.J., Cotton, W.D., Greisen, E.W., Yin, Q.F., Perley, R.A., Taylor, G.B., & Broderick, J.J. 1998, *AJ*, 115, 1693
- Egan, M.P., Shipman, R.F., Price, S.D., Carey, S.J., Clark, F.O., & Cohen, M. 1998, *ApJ*, 494, L199
- Faúndez, S., Bronfman, L., Garay, G., Chini, R., Nyman, L.-Å., & May, J. 2004, *A&A*, 426, 97
- Garay, G. 2005, in *Massive star birth: A crossroads of Astrophysics, Proceedings IAU Symposium No. 227*, eds. Cesaroni, R., Felli, M., Churchwell, E., Walmsley, M. (Cambridge: Cambridge University Press), 86
- Garay, G., Brooks, K.J., Mardones, D., & Norris, R.P. 2006, submitted to *ApJ*. (Paper I)
- Garay, G., Brooks, K.J., Mardones, D., Norris, R. P. & Burton, M.G. 2002, *ApJ*, 579, 678
- Garay, G., Faúndez, S., Mardones, D., Bronfman, L., Chini, R., & Nyman, L.-Å. 2004, *ApJ*, 610, 313
- Juvela, M. 1996, *A&AS*, 118, 191
- Keto, E. 2002, *ApJ* 580, 980

- Mardones, D. 1998, Ph.D. thesis, Harvard University
- McKee, C.F., & Tan, J. C. 2002, *Nature* 416, 59
- McKee, C.F., & Tan, J. C. 2003, *ApJ*, 585, 850
- Megeath, S.T., Herter, T., Beichman, C., Gautier, N., Hester, J.J., Rayner, J., & Shupe, D. 1996, *A&A*, 307, 775
- Menten, K.M., Pillai, T., & Wyrowski, F. 2005, in *Massive star birth: A crossroads of Astrophysics*, Proceedings IAU Symposium No. 227, eds. Cesaroni, R., Felli, M., Churchwell, E., Walmsley, M. (Cambridge: Cambridge University Press), 23
- Molinari, S., Testi, L., Rodríguez, L.F., & Zhang, Q. 2002, *ApJ*, 570, 758
- Motte, F., & André, P. 2001, *A&A*, 365, 440
- Mueller, K.E., Shirley, Y.L., Evans II, N.J. & Jacobson, H.R. 2002, *ApJS*, 143, 469
- Orosio, M., Lizano, S., & D'Alessio, P. 1999, *ApJ*, 525, 808
- Ossenkopf, V., & Henning, Th. 1994, *A&A*, 291, 943
- Plume, R., Jaffe, D.T., & Evans II, N.J. 1992, *ApJS*, 78, 505
- Plume, R., Jaffe, D.T., Evans II, N.J., Martín-Pintado, J. & Gómez-González, J. 1997, *ApJ*, 476, 730
- Price, S.D. 1995, *Space Sci. Rev.*, 74, 81
- Shirley, Y.L., Evans II, N.J., Young, K.E., Knez, C., & Jaffe, D.T. 2003, *ApJS*, 149, 375
- Sridharan, T.K., Beuther, H., Saito, M., Wyrowski, F., & Schilke, P. 2005, *ApJ*, 634, L57
- Stahler, S.W., Palla, F., & Ho, P.T.P. 2000, *Protostars and Planets IV*, ed. V. Mannings, A.P. Boss, & S.S. Russell (Tucson: Univ. Arizona), 327
- van der Tak, F.F.S., van Dishoeck, E.F., Evans II, N.J., & Blake, G.A. 2000, *ApJ*, 537, 283
- Williams, S.J., Fuller, G.A., & Sridharan, T.K. 2004, *A&A*, 417, 115
- Williams, S.J., Fuller, G.A., & Sridharan, T.K. 2005, *A&A*, 434, 257
- Yorke, H.W., & Sonnhalter, C. 2002, *ApJ*, 569, 846

Table 1. OBSERVED SOURCES

IRAS source	Galactic name	Observed central position		Noise (mJy beam ⁻¹)
		α (J2000) h m s	δ (J2000) ° ' "	
12383-6128	G301.731 + 1.104	12 41 17.4	-61 44 40	28
13291-6249	G307.560 - 0.586	13 32 30.4	-63 05 19	38
14095-6102	G312.596 + 0.048	14 13 13.9	-61 16 48	66
14593-5852	G319.163 - 0.419	15 03 13.2	-59 04 24	63
15394-5358	G326.474 + 0.697	15 43 17.7	-54 07 30	61
15502-5302	G328.307 + 0.432	15 54 06.0	-53 11 38	50
15520-5234	G328.808 + 0.632	15 55 48.4	-52 43 10	42
15596-5301	G329.404 - 0.457	16 03 31.2	-53 09 29	40
16128-5109	G332.153 - 0.445	16 16 39.3	-51 16 58	85
16272-4837	G335.582 - 0.284	16 30 56.5	-48 43 46	37
16458-4512	G340.248 - 0.373	16 49 30.2	-45 17 50	36
16524-4300	G342.704 + 0.130	16 56 04.0	-43 04 43	37
16547-4247	G343.126 - 0.062	16 58 16.9	-42 52 07	45
17008-4040	G345.499 + 0.354	17 04 23.1	-40 44 26	59
17009-4042	G345.490 + 0.311	17 04 26.9	-40 46 27	59
17016-4124	G345.001 - 0.220	17 05 09.8	-41 29 04	44
17158-3901	G348.534 - 0.973	17 19 16.1	-39 04 26	38
17271-3439	G353.416 - 0.367	17 30 26.5	-34 41 39	40

Table 2. OBSERVED PARAMETERS OF OVERALL 1.2-MM EMISSION

SIMBA source	Peak position		Flux density ^a		Angular size ^b (")	Morphology
	$\alpha(2000)$	$\delta(2000)$	Peak (Jy/beam)	Total (Jy)		
12383-6128	12 41 17.6	-61 44 43	1.15	13.4	116 × 72	multiple
13291-6249	13 32 31.2	-63 05 23	2.33	8.5	32 × 31	compact+irreg.
14095-6102	14 13 15.0	-61 16 57	1.99	6.7	40 × 26	c+e
14593-5852	15 03 13.8	-59 04 36	1.79	11.3	81 × 50	multiple
15394-5358	15 43 16.9	-54 07 15	5.18	15.9	42 × 24	c+e
15502-5302	15 54 06.2	-53 11 37	5.57	27.3	48 × 31	c+e
15520-5234	15 55 48.8	-52 43 06	9.92	27.0	28 × 22	c+e
15596-5301	16 03 32.1	-53 09 28	2.45	8.3	39 × 28	c+e
16128-5109	16 16 40.5	-51 17 04	2.74	19.9	82 × 56	c+e
16128-West	16 16 16.0	-51 18 16	1.98	6.8	48 × 41	Gaussian
16272-4837	16 30 58.7	-48 43 53	5.09	13.9	33 × 22	c+e
16458-4512	16 49 30.1	-45 17 52	2.31	14.7	76 × 47	multiple
16524-4300	16 56 02.7	-43 04 48	2.46	11.1	47 × 45	c+e
16547-4247	16 58 17.2	-42 52 04	7.33	20.8	34 × 25	c+e
17008-4040	17 04 22.8	-40 44 21	5.77	34.1	102 × 57	c+e
17009-4042	17 04 27.7	-40 46 26	9.38	44.8	49 × 34	Gaussian
17016-4124	17 05 11.1	-41 29 03	8.42	45.0	—	core+filament
17016-South	17 05 22.0	-41 31 14	0.69	6.5	89 × 85	irregular
17158-3901	17 19 20.5	-39 03 52	2.97	26.7	129 × 73	multiple
17271-3439	17 30 26.5	-34 41 45	9.86	89.0	87 × 49	core-halo

^aErrors in the flux density are dominated by the uncertainties in the flux calibration, of $\sim 20\%$.

^bErrors in the angular sizes are typically 10%.

Table 3. OBSERVED PARAMETERS OF INDIVIDUAL 1.2-MM COMPONENTS

SIMBA source	Peak position		Flux density		Angular size (")
	$\alpha(2000)$	$\delta(2000)$	Peak (Jy/beam)	Total (Jy)	
12383-6128 A	12 41 02.7	-61 44 19	0.34	1.2	59×41
12383-6128 B	12 41 10.3	-61 45 05	0.49	0.6	37×18
12383-6128 C	12 41 17.7	-61 44 38	1.15	2.3	57×20
12383-6128 D	12 41 22.2	-61 44 56	0.90	2.1	46×28
12383-6128 halo	12 41 17.0	-61 44 26	–	~ 7	212×116
14593-5852-A	15 03 11.7	-59 04 42	1.08	10.1	90×54
14593-5852-B	15 03 13.8	-59 04 36	1.79	0.88	– ^a
16458-4512 A	16 49 26.2	-45 18 09	0.82	1.31	23×14
16458-4512 B	16 49 30.4	-45 17 53	2.31	10.3	52×44
17016-4124-core	17 05 11.1	-41 29 03	8.42	13.7	24×21
17016-4124-fila	17 05 12.2	-41 28 28	0.80	33.9	308×95
17158-3901 A	17 19 15.7	-39 04 34	2.02	11.2	179×35
17158-3901 B	17 19 18.4	-39 04 47	1.99	11.5	76×49
17158-3901 C	17 19 20.5	-39 03 52	2.97	6.3	30×24
17271-3439 core	17 30 26.5	-34 41 45	9.86	18.2	37×21
17271-3439 halo	17 30 26.1	-34 41 40	–	65.4	169×84

^aunresolved.

Table 4. DERIVED PARAMETERS

SIMBA source	D (kpc)	T_d (K)	Radius (pc)	Mass (M_\odot)	$n(\text{H}_2)$ (cm^{-3})	$N(\text{H}_2)$ (cm^{-2})	$\tau_{1.2\text{mm}}$
12383-6128	4.4	24.	0.93	3.4×10^3	1.7×10^4	6.7×10^{22}	0.0026
13291-6249	2.8	29.	0.21	5.2×10^2	2.2×10^5	1.9×10^{23}	0.0075
14095-6102	5.7	28.	0.44	2.2×10^3	1.0×10^5	1.9×10^{23}	0.0075
14593-5852	11.5	27.	1.73	1.5×10^4	1.2×10^4	8.6×10^{22}	0.0034
15394-5358	2.8	25.	0.22	1.5×10^3	5.9×10^5	5.3×10^{23}	0.0209
15502-5302	5.6	41.	0.52	4.6×10^3	1.4×10^5	2.9×10^{23}	0.0114
15520-5234	2.9	42.	0.17	1.5×10^3	1.2×10^6	8.6×10^{23}	0.0341
15596-5301	4.6	28.	0.37	1.8×10^3	1.4×10^5	2.2×10^{23}	0.0087
16128-5109	3.7	33.	0.58	2.1×10^3	4.3×10^4	1.0×10^{23}	0.0041
16272-4837	3.4	25.	0.22	2.1×10^3	8.0×10^5	7.2×10^{23}	0.0286
16458-4512	3.8	26.	0.52	2.1×10^3	6.1×10^4	1.3×10^{23}	0.0052
16524-4300	3.6	27.	0.54	1.5×10^3	4.0×10^4	8.8×10^{22}	0.0035
16547-4247	2.9	31.	0.20	1.9×10^3	9.3×10^5	7.7×10^{23}	0.0305
17008-4040	2.0	30.	0.36	1.2×10^3	1.1×10^5	1.6×10^{23}	0.0065
17009-4042	2.1	32.	0.21	1.6×10^3	7.2×10^5	6.3×10^{23}	0.0247
17016-4124	2.7	30.	0.22	1.8×10^3	6.7×10^5	6.1×10^{23}	0.0240
17158-A	2.0	28.	0.38	5.0×10^2	3.6×10^4	5.7×10^{22}	0.0022
17158-B	2.0	28.	0.29	5.1×10^2	8.1×10^4	9.9×10^{22}	0.0039
17158-C	2.0	28.	0.13	2.8×10^2	5.3×10^5	2.8×10^{23}	0.0111
17271-3439	4.5	35.	0.72	1.4×10^4	1.6×10^5	4.8×10^{23}	0.0188

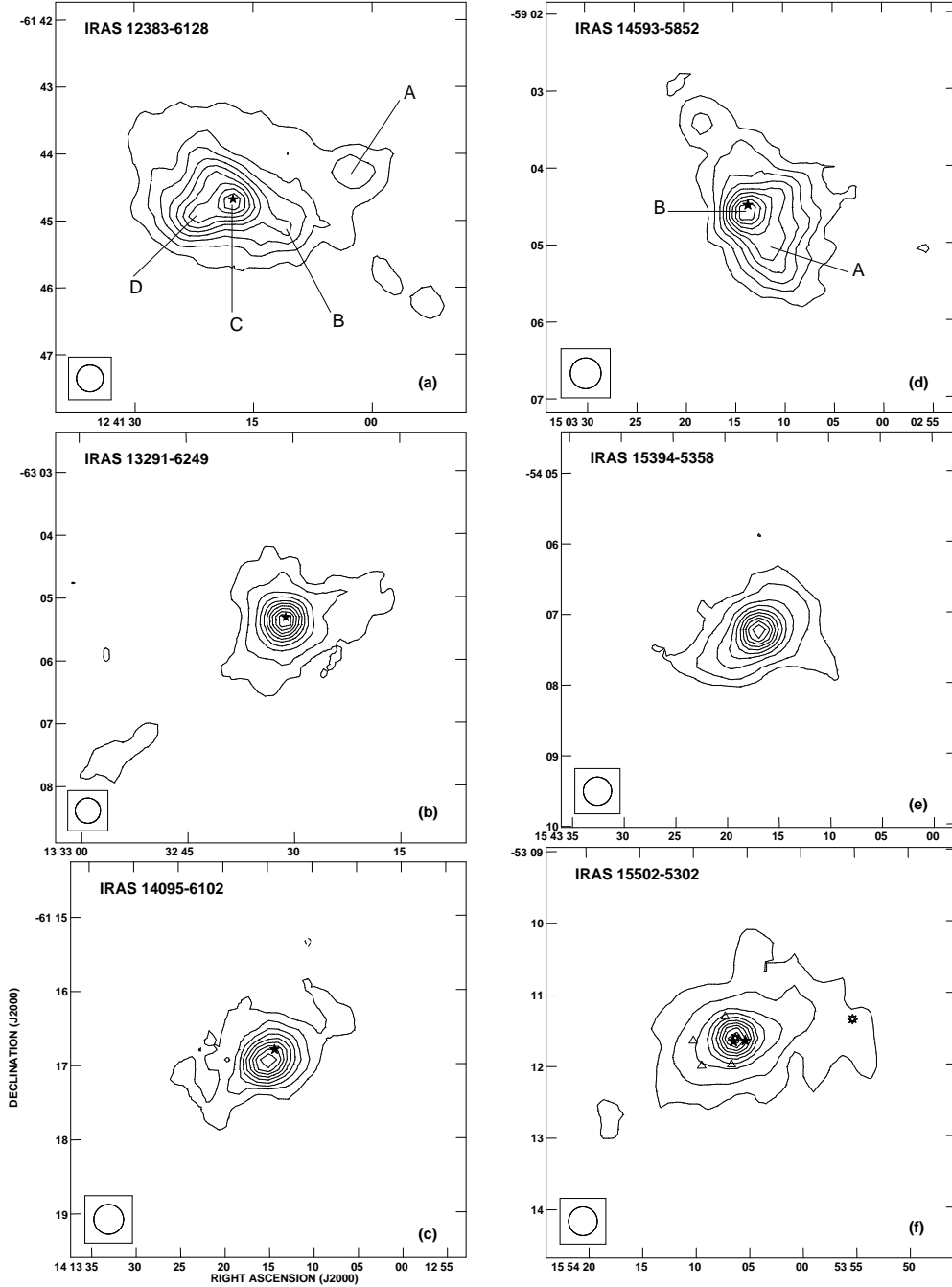


Fig. 1.— SEST/SIMBA maps of the 1.2-mm dust continuum emission towards young massive star forming regions. FWHM beams are shown in the lower left corner. Contour levels are either: (i) -10, 10 to 90 by 10 percent; (ii) -5, 5, 10 to 90 by 10 percent; or (iii) -2.5, 2.5, 5, 10 to 90 by 10 percent, of the observed peak flux density. (a) IRAS 12383–6128. Contour levels (i). Peak flux density $1.15 \text{ Jy beam}^{-1}$; (b) IRAS 13291-6249. Contour levels (ii). Peak flux density $2.33 \text{ Jy beam}^{-1}$; (c) IRAS 14095-6102. Contour levels (i). Peak flux density $1.99 \text{ Jy beam}^{-1}$; (d) IRAS 14593-5852. Contour levels (i). Peak flux density $1.79 \text{ Jy beam}^{-1}$; (e) IRAS 15394-5358. Contour levels (ii). Peak flux density $5.18 \text{ Jy beam}^{-1}$; (f) IRAS 15502-5302. Contour levels (ii). Peak flux density $5.57 \text{ Jy beam}^{-1}$.

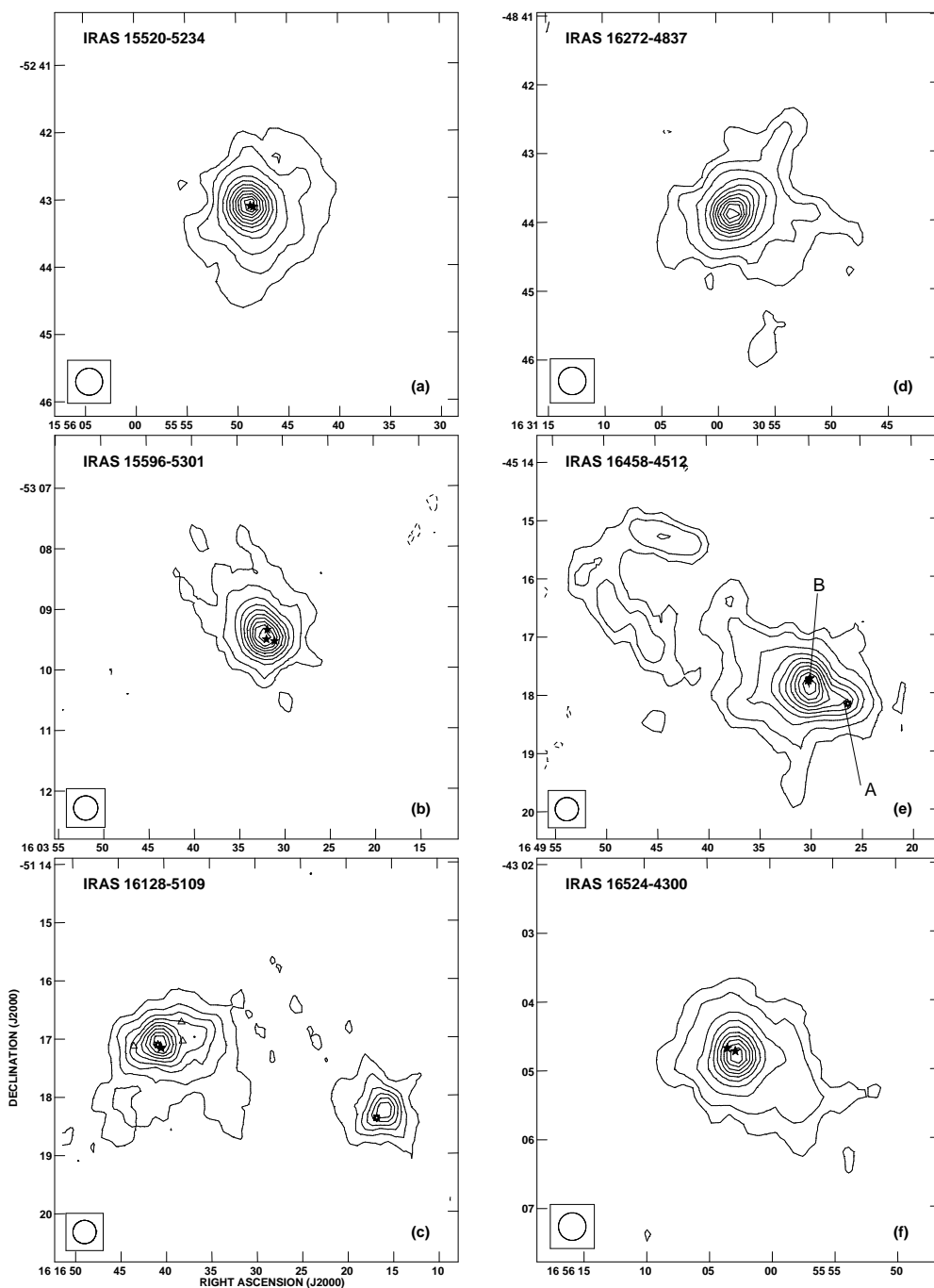


Fig. 2.— Same as in Fig. 1. Panel (a) IRAS 15520-5234. Contour levels (iii). Peak flux density $9.92 \text{ Jy beam}^{-1}$. Panel (b) IRAS 15596-5301. Contour levels (ii). Peak flux density $2.45 \text{ Jy beam}^{-1}$. Panel (c) IRAS 16128-5109. Contour levels (i). Peak flux density $2.74 \text{ Jy beam}^{-1}$. Panel (d) IRAS 16272-4837. Contour levels (iii). Peak flux density $5.09 \text{ Jy beam}^{-1}$. Panel (e) IRAS 16458-4512. Contour levels (ii). Peak flux density $2.31 \text{ Jy beam}^{-1}$. Panel (f) IRAS 16524-4300. Contour levels (ii). Peak flux density $2.46 \text{ Jy beam}^{-1}$.

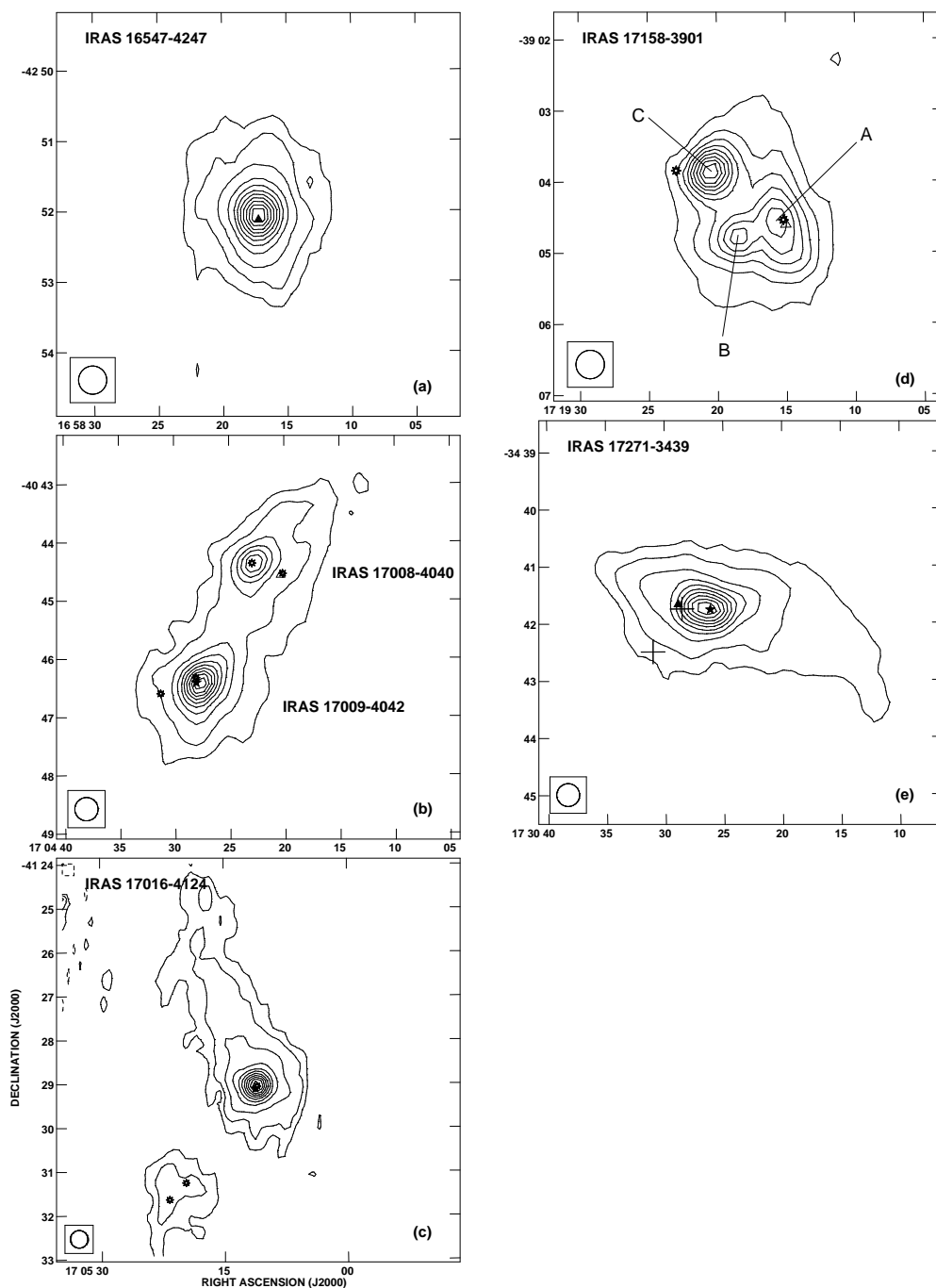


Fig. 3.— Same as in Fig. 1. Panel (a) IRAS 16547-4247. Contour levels (iii). Peak flux density $7.33 \text{ Jy beam}^{-1}$. Panel (b) IRAS 17008-4040 and IRAS 17009-4042. Contour levels (ii). Peak flux density $9.38 \text{ Jy beam}^{-1}$. Panel (c) IRAS17016-4124. Contour levels (iii). Peak flux density $8.42 \text{ Jy beam}^{-1}$. Panel (d) IRAS 17158-3901. Contour levels (i). Peak flux density $2.97 \text{ Jy beam}^{-1}$. Panel (e) IRAS 17271-3439. Contour levels (ii). Peak flux density $9.86 \text{ Jy beam}^{-1}$.

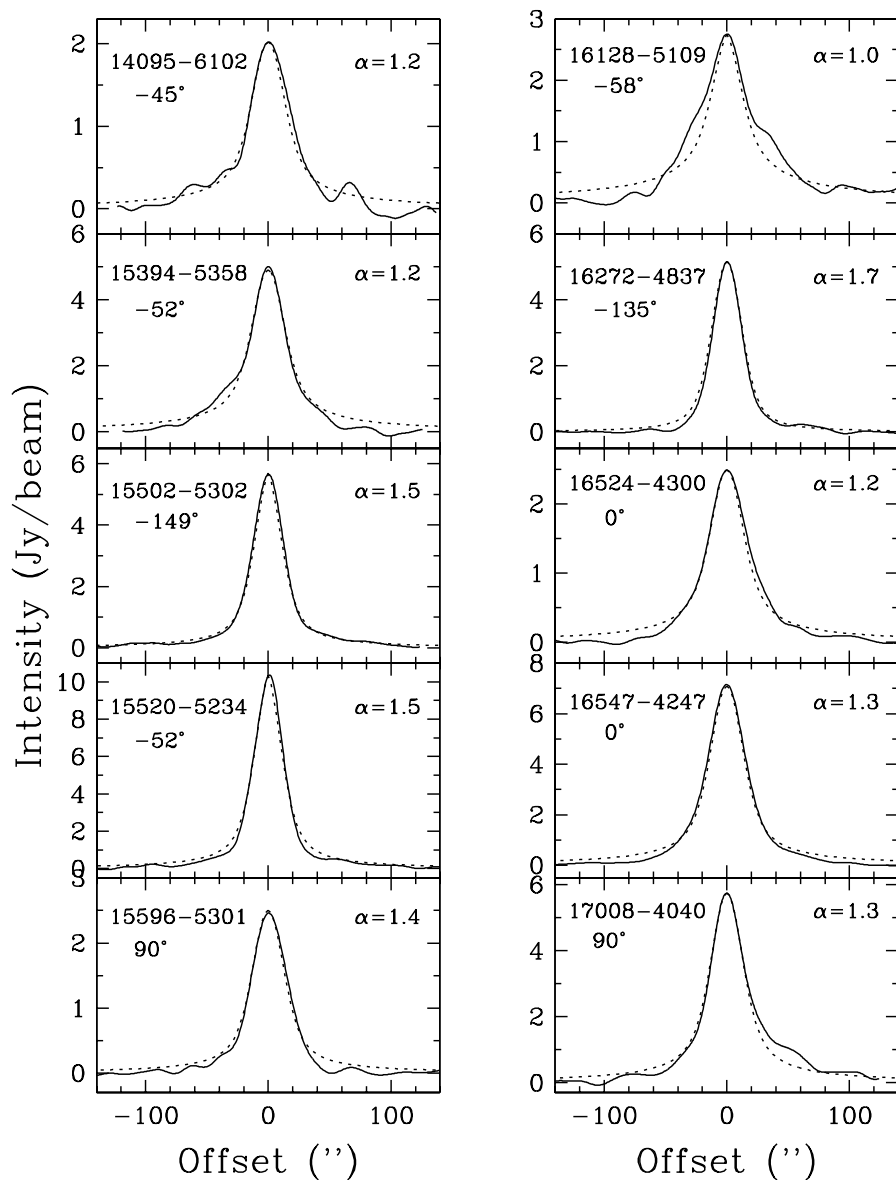


Fig. 4.— Intensity cuts across 1.2-mm sources with core-halo morphologies. The source name and position angle of the slice, which passes through the source peak position, are given in the upper left corner. Dotted lines correspond to fits of the observed radial intensity with single power-law intensity profiles. The fitted power-law indices are given in the upper right corner.

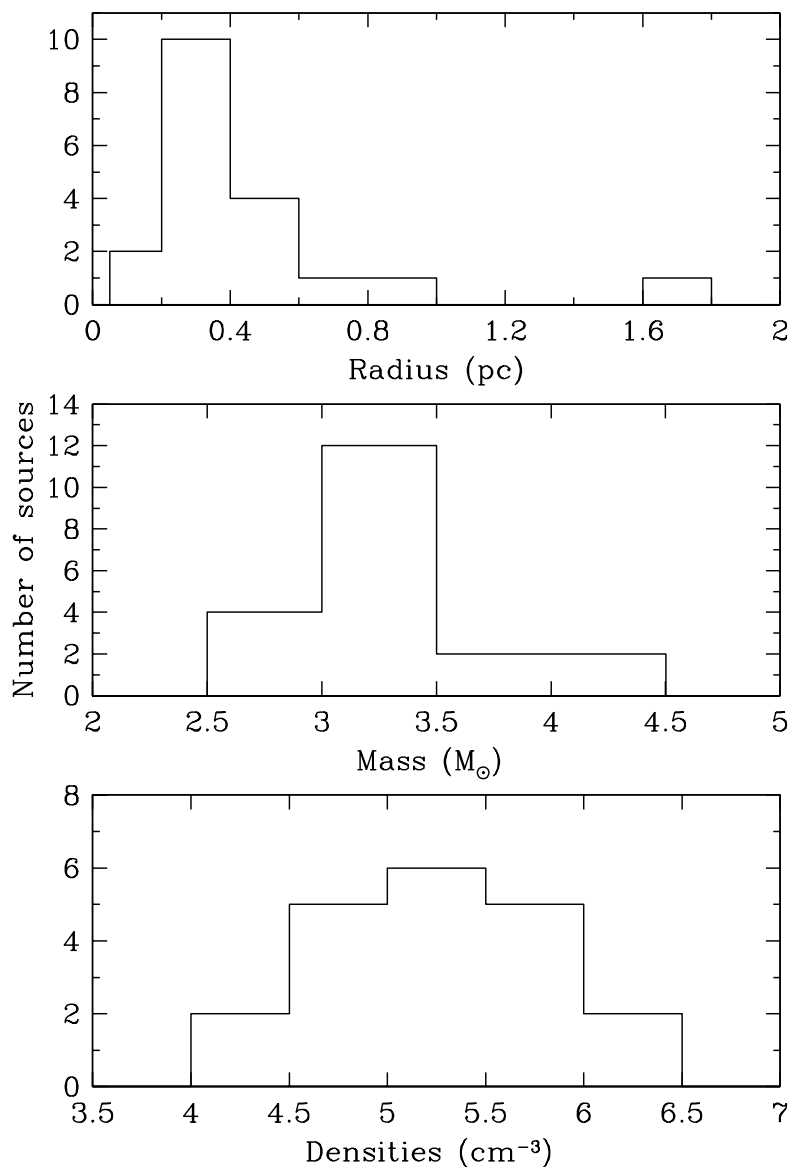


Fig. 5.— Distribution of parameters of 1.2-mm cores associated with young high-mass star forming regions. Top: Size distribution. Average and median radius are 0.38 and 0.36 pc, respectively. Middle: Mass distribution. Average and median mass are 2.4×10^3 and $1.8 \times 10^3 M_{\odot}$, respectively. Bottom: Density distribution. Average and median density are 3.5×10^5 and $1.4 \times 10^5 \text{ cm}^{-3}$, respectively.

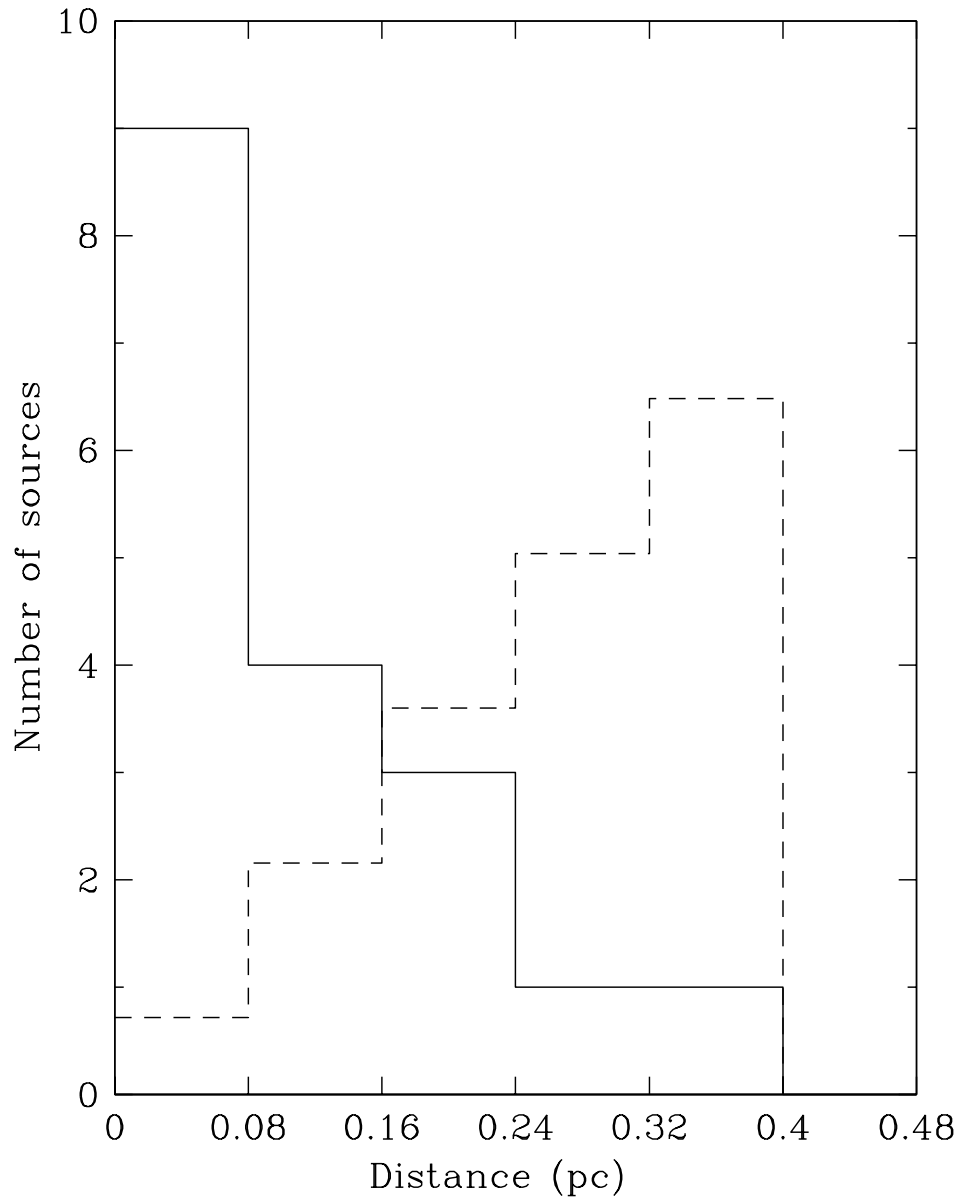


Fig. 6.— Distribution of the distance of compact H II regions from the peak position of the associated 1.2-mm dust core (continuous line). The dotted line indicates the expected distribution if the regions of ionized gas were uniformly distributed across the core.